


Magnon junction effect induced by bulk acoustic wavesHanbing Ling¹,[✉] Liang Wang,¹ Lisha Wang,¹ Syed UI Hasnain Bakhtiar,¹ Zhao Ye,¹
Tao Wang,¹ Yue Zhang,^{1,*} and Qiuyun Fu^{1,2,†}¹Engineering Research Center for Functional Ceramics of Ministry of Education, School of Integrated Circuits,
Huazhong University of Science and Technology, Wuhan 430074, China²Shenzhen Huazhong University of Science and Technology Research Institute, Shenzhen 518000, China (Received 27 October 2022; revised 2 October 2023; accepted 19 October 2023; published 2 November 2023)

As an analog to a magnetic tunneling junction, a magnon junction composed of a ferromagnetic insulator (FMI)/antiferromagnetic insulator (AFMI)/ferromagnetic insulator heterostructure has been proposed in recent years. In a magnon junction, the magnon current transmission can be adjusted by manipulating the angle of magnetic moments in the two FM layers. However, the mechanism of this magnon junction effect is still not quite clear. In this paper, we numerically calculate the bulk acoustic wave-induced magnon junction effect. Our results emphasize the crucial role played by variations in magnetic structures within the AFMI spacer when the alignments of magnetic moments in the two FMI layers are adjusted between the parallel and antiparallel state. These differences significantly influence the modulation of magnon current transmission. This is different from the chirality-relevant magnon scattering mechanism as assumed in previous works.

DOI: [10.1103/PhysRevB.108.174404](https://doi.org/10.1103/PhysRevB.108.174404)**I. INTRODUCTION**

Spin valves (SVs) and magnetic tunneling junctions (MTJs), which consist of a nonmagnetic layer sandwiched between two ferromagnetic metallic (FM) layers, play a crucial role in transferring electrical spin current controlled by the angle of the magnetic moments in the two FM layers [1–3]. Apart from electron-based spin transfer, researchers have extensively explored magnon current transmission in magnetic insulators such as $\text{Y}_3\text{Fe}_5\text{O}_{12}$ (YIG). The compelling advantages of this magnon device include minimal Joule dissipation and long transmission distances.

As an analog to SVs, a magnon valve using a YIG/Au/YIG structure was proposed in 2018 [4]. In such a magnon valve, magnon current transmission between two YIG layers can be adjusted by the relative orientations of magnetic moments in the two YIG layers [4]. However, a significant challenge remained: a limited conversion between the magnon and charge current at the interface between the ferromagnetic insulator (FMI) and metal layers. To overcome this problem, an all-insulating YIG/NiO/YIG magnon junction has been developed with a magnon current generated by a longitudinal spin Seebeck effect [5]. In this magnon junction, the magnon current is able to pass through the NiO when the magnetic moments in the two YIG layers are parallel but almost totally blocked when they are antiparallel, giving rise to a high magnon blocking ratio (MBR) of about 100% [6]. Even though the discovery of the magnon junction effect has opened up a field for low-dissipation magnonic devices, the physical mechanism for this magnon junction effect is still

not quite clear. Analogous to the physical principle underlying the magnetoresistance effect in SVs and MTJs, the magnon junction effect is attributed to the manipulation of magnon transmission along distinct paths within the antiferromagnetic insulator (AFMI) with differing chiralities for spin oscillations [6]. However, the observation of magnon current transmission in a very thin AFMI spacer is still rather challenging.

In this paper, we propose a differential explanation for the magnon junction effect based on a numerical investigation of the acoustic wave-induced magnon junction effect (Fig. 1). Our work reveals that the distinct magnetic-moment alignment within the AFMI layer between the parallel and antiparallel alignments of magnetic moments in the two FM layers plays a critical role in controlling the transmission of magnon current throughout the junction. This is different from the chirality-relevant magnon scattering principle [6].

II. MODEL AND METHOD

Our study exploits the numerical method proposed by Azovtsev and Pertsev for the simulation of magnetic oscillation within an FM medium driven by an acoustic wave [7–9]. To generate a bulk acoustic wave, we applied an alternating voltage on a piezoelectric transducer [10–14]. This voltage induces a longitudinal displacement (u_z) given by $u_z = dU_{\max} \sin(2\pi ft)$. Here, d is the piezoelectric strain constant, f is the linear frequency for the alternating acoustic wave, and U_{\max} is the amplitude of the voltage.

The AFMI spacer in the magnon junction is composed of two sublattices, labeled A and B . The direction of the magnetic moments in FMI1 is fixed, while that of FMI2 can be parallel (P) or antiparallel (AP) to the magnetic moments in FMI1. We consider a magnon junction CoFe_2O_4 (CFO) 1(20)/NiO(20)/CFO2(20) with 20 denoting the number of the

*Corresponding author: yue-zhang@hust.edu.cn†Corresponding author: fuqy@mail.hust.edu.cn

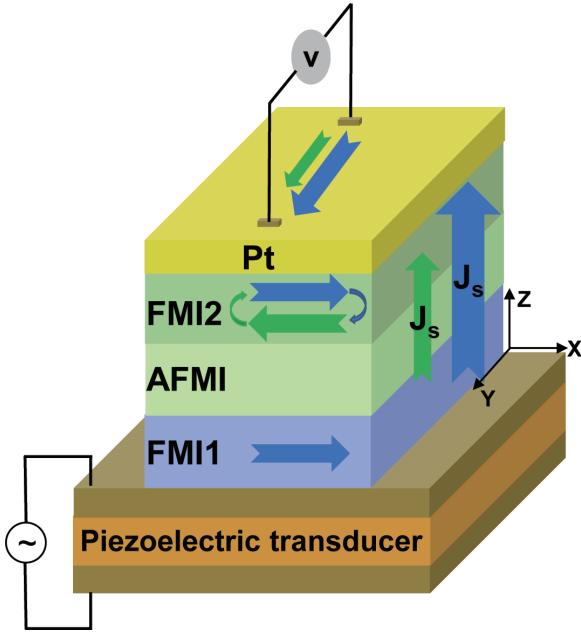


FIG. 1. Schematic of the magnon junction effect induced by a bulk acoustic wave. A bulk acoustic wave was generated at a piezoelectric transducer and transmitted to the adjacent FMI medium. A magnon current was generated in the FMI layer under magnetoelastic coupling, and it transports through the AFMI spacer and eventually penetrates into the other FMI layer to produce an inverse spin Hall effect voltage in the top heavy metal (Pt) layer. When the magnetic moments in the two FMI layers are parallel (antiparallel) aligned, a strong (weak) spin current can transmit through the AFMI spacer.

unit cells of magnetic moments aligning along the z direction. Based on the lattice constants of CFO (0.84 nm) and NiO (0.42 nm), the thicknesses of CFO and NiO are approximately 17 and 8 nm, respectively. The fabrication of the multilayer with these thicknesses is experimentally feasible [4,5,15–18]. In the xy plane, we employed 6×6 unit cells with a periodic boundary condition [6,19,20]. To avoid magnon current reflection at the surface, we incorporate a high damping coefficient region near the surface of the magnon junction.

The calculation is based on the atomistic simulation by numerically solving the Landau-Lifshitz-Gilbert (LLG) equation

$$\frac{\partial \mathbf{S}_i}{\partial t} = -\frac{\gamma}{1 + \alpha^2} [\mathbf{S}_i \times \mathbf{H}_{\text{eff}}^i + \alpha \mathbf{S}_i \times (\mathbf{S}_i \times \mathbf{H}_{\text{eff}}^i)], \quad (1)$$

where \mathbf{S}^i symbolizes the normalized magnetic moment at the i th unit cell. $\gamma = 2.21 \times 10^5$ m/A s is the gyromagnetic ratio of electrons, α is the Gilbert damping coefficient, and $\mathbf{H}_{\text{eff}}^i$ is the total effective magnetic field given by $\mathbf{H}_{\text{eff}}^i = \partial E / \partial \mathbf{S}^i$ with the total energy E expressed as

$$E = E_{\text{ex}} + E_{\text{ani}} + E_{\text{ext}} + E_{\text{dip}} + E_{\text{mel}}, \quad (2)$$

$$E_{\text{ex}} = -J_{\text{FM}} \sum_{\langle i,j \rangle} \mathbf{S}^i \cdot \mathbf{S}^j - J_{\text{AFM}} \sum_{\langle m,n \rangle} \mathbf{S}^m \cdot \mathbf{S}^n - J_{\text{FM-AFM}} \sum_{\langle i,m \rangle} \mathbf{S}^i \cdot \mathbf{S}^m, \quad (3)$$

$$E_{\text{ani}} = -K_u \sum_{\langle i \rangle} [(\mathbf{S}^i \cdot \mathbf{e}_x)^2], \quad (4)$$

$$E_{\text{ext}} = -\sum_{\langle i \rangle} (\mu_s \mathbf{S}^i \cdot \mathbf{H}_{\text{ext}}), \quad (5)$$

$$E_{\text{dip}} = -\frac{g^2 \mu_B^2}{a_0^3} \left(\frac{a_0}{r_{ij}} \right)^3 \sum_{\langle i \neq j \rangle} [3(\mathbf{S}^i \cdot \mathbf{e}^{ij})(\mathbf{S}^j \cdot \mathbf{e}^{ij}) - (\mathbf{S}^i \cdot \mathbf{S}^j)], \quad (6)$$

$$E_{\text{mel}} = -\sum_{\langle i \rangle} \left(B_1 \sum_{\langle s \rangle} (\mathbf{S}_s^i)^2 \epsilon_{ss} + B_2 \sum_{\langle s \neq p \rangle} S_s^i S_p^i \epsilon_{sp} \right), \quad (7)$$

where \mathbf{S}^o ($o = i, j, m, n$) is the normalized spin magnetic moment at site o (i or j belong to FM, and m or n belong to AFM), and $S_{s(p)}^i$ ($s, p = x, y, z$) is the $s(p)$ component of \mathbf{S}^i . E_{ex} denotes the exchange energy, J_{FM} and J_{AFM} are the nearest-neighbor exchange interaction energies within FMI and AFMI, respectively. For CFO and NiO, $J_{\text{FM}} = 3.69 \times 10^{-16}$ ergs and $J_{\text{AFM}} = -1.47 \times 10^{-15}$ ergs, respectively [6,9,21,22]. Completely uncompensated interfaces were considered, and the exchange energy at the FMI/AFMI interface was calculated based on a harmonic mean exchange energy as $J_{\text{FM-AFM}} = 2J_{\text{FM}}|J_{\text{AFM}}|/(J_{\text{FM}} + |J_{\text{AFM}}|)$ [19,23,24]. E_{ani} signifies the magnetic anisotropy energy, where K_u is the atomistic uniaxial magnetic anisotropy energy. For CFO and NiO, $K_{u(\text{CFO})} = 5.91 \times 10^{-17}$ ergs and $K_{u(\text{NiO})} = 1.48 \times 10^{-17}$ ergs, respectively [9,20,21]. Here, \mathbf{e}_x is the unit vector along the easy axis x . E_{ext} represents the Zeeman energy under an external magnetic field with μ_s and \mathbf{H}_{ext} the atomic spin moment and the external magnetic field, respectively [20]. E_{dip} corresponds to the magnetic dipole-dipole interaction with g the electron g factor, μ_B the Bohr magneton, a_0 the Bohr radius (0.052 917 7 nm), r^{ij} the distance between lattice sites i and j , and \mathbf{e}^{ij} the unit vector along the direction pointing from site i to j [25,26]. E_{mel} indicates the magnetoelastic energy with $B_1 = 3.49 \times 10^{-13}$ ergs and $B_2 = -2.13 \times 10^{-13}$ ergs the first- and second-order magnetoelastic energies, respectively [9,27]. The normal components of the strain tensor are denoted by ϵ_{xx} , ϵ_{yy} , ϵ_{zz} , while ϵ_{xy} , ϵ_{yz} , ϵ_{zx} represent the shear components.

A bulk acoustic wave was applied to the magnon junction, and the strain can be expressed as $\epsilon_{zz} = u_z 2\pi f / \sqrt{C_{11}^F / \rho_F}$, where C_{11}^F and ρ_F represent the elastic stiffness constant and mass density of FMI, respectively. For CFO, $C_{11}^F = 2.57 \times 10^{12}$ dyn/cm² and $\rho = 5.294$ g/cm³. The maximum u_z^{max} is 2.23×10^{-2} nm, which gives rise to the strain ϵ_{zz} of 2×10^{-4} .

Equation (1) was numerically solved using the fourth-order Runge-Kutta method with a 0.1 ps time step. Considering that the initial magnetic moment is oriented along the x axis, we introduced an external magnetic field $H_z = 1000$ Oe and $H_y = 100$ Oe so that the magnetic oscillation can be triggered. Based on the numerical solution of Eq. (1), we further derived the spin current density at different positions. In the FMI layer, the spin current density was calculated based on the definition of an exchange spin current, $J_m^z = A_{\text{ex}} \mathbf{m} \times \frac{\partial \mathbf{m}}{\partial z}$, where A_{ex} is the exchange constant and $\mathbf{m}(z) = \frac{1}{N} \sum_{\langle i \in z \rangle} \mathbf{S}_i$ (the magnetization of monolayer along the z direction, and N is the number of spins per layer) [19,28]. In a collinear AFMI medium, the spin current density was quantified by the Néel vector $\mathbf{n} = (\mathbf{m}_A - \mathbf{m}_B)/2$ as $J_m^z = \gamma A_{\text{n}} \times \frac{\partial \mathbf{n}}{\partial z}$, where

$\mathbf{m}_{A(B)}$ corresponds to sublattice magnetizations [29–33]. Here, γ and A are the gyromagnetic ratio of an electron and the inhomogeneous exchange constant, respectively [34]. On the other hand, at the interface between FMI2 and the heavy metal (Pt) layer, a magnon current can penetrate into the Pt layer due to spin pumping [35,36]. The spin current density at the FMI2/Pt interface was formulated as in Eq. (8), which can be simplified to Eq. (9) as the imaginary components of the reflection and transmission of spin-mixing conductance in insulator-metal contacts are often negligible [9,37,38],

$$\mathbf{J}_s = \frac{\hbar}{4\pi} \left(\text{Re}[g'_{\uparrow\downarrow} - g'_{\downarrow\uparrow}] \mathbf{m} \times \frac{d\mathbf{m}}{dt} + \text{Im}[g'_{\uparrow\downarrow} - g'_{\downarrow\uparrow}] \frac{d\mathbf{m}}{dt} \right), \quad (8)$$

$$\mathbf{J}_s \cong \frac{\hbar}{4\pi} \text{Re}[g'_{\uparrow\downarrow}] \mathbf{m} \times \frac{d\mathbf{m}}{dt}, \quad (9)$$

where $g'_{\uparrow\downarrow}$ and $g'_{\downarrow\uparrow}$ are the complex reflection and transmission of spin-mixing conductance, respectively.

The spin current flowing into the Pt layer can be further transformed into a transversal electrical current due to the inverse spin Hall effect, which can generate a voltage (U_{ISHE}) as shown in Eq. (10) [39,40]. Here, the parameters w , α_{SH} , λ , d , and σ represent the length, spin Hall angle, spin diffusion length, thickness, and conductivity of Pt, respectively [37,38],

$$U_{\text{ISHE}} = \frac{2e}{\hbar} \frac{w \alpha_{\text{SH}} \lambda}{d \sigma} \tanh\left(\frac{d}{2\lambda}\right) \bar{J}_s, \quad (10)$$

where \bar{J}_s is the average direct current (dc) component of the spin current density. Based on the difference of U_{ISHE} between the parallel and antiparallel alignments of the magnetic moments in the two FMI layers, the magnon junction efficiency can be quantified by using the MBR defined as $\text{MBR} = (U_{\uparrow\uparrow} - U_{\uparrow\downarrow})/U_{\uparrow\uparrow}$. Here, $U_{\uparrow\uparrow}$ ($U_{\uparrow\downarrow}$) signifies the U_{ISHE} for the parallel (antiparallel) state [6]. The MBR serves as a quantitative index of the magnon junction efficiency.

The U_{ISHE} was calculated based on the following parameters: The spin Hall angle and conductivity of Pt is 0.056, and 9.35×10^6 S/m, respectively. The real part of the spin-mixing conductance at the CFO/Pt interface is $\text{Re}[g'_{\uparrow\downarrow}] = 0.62 \times 10^{19} \text{ m}^{-2}$ [9]. The length and thickness of the Pt layer is 1000 μm and 10 nm, respectively.

III. RESULTS AND DISCUSSION

Our study considers the magnon current in a CFO/NiO/CFO junction, driven by a bulk acoustic wave. In a ferrimagnetic material such as CFO, the magnetic moments of the two sublattices align in opposite directions but with unequal magnitudes, leading to a nonzero net magnetic moment. The dynamics of magnon currents at ultrahigh frequencies (hundreds of GHz or higher) include the exchange coupling between the two sublattices [41]. Nevertheless, at low frequencies, such as the 10 GHz utilized in our study, the ferrimagnetic spin dynamics are analogous to those of a ferromagnetic counterpart [41,42]. Therefore, we treat CFO as a ferromagnetic medium composed by the net magnetic moment.

We considered the AFMI spacer with two structural types (types A and C in Fig. 2), corresponding to the alignment

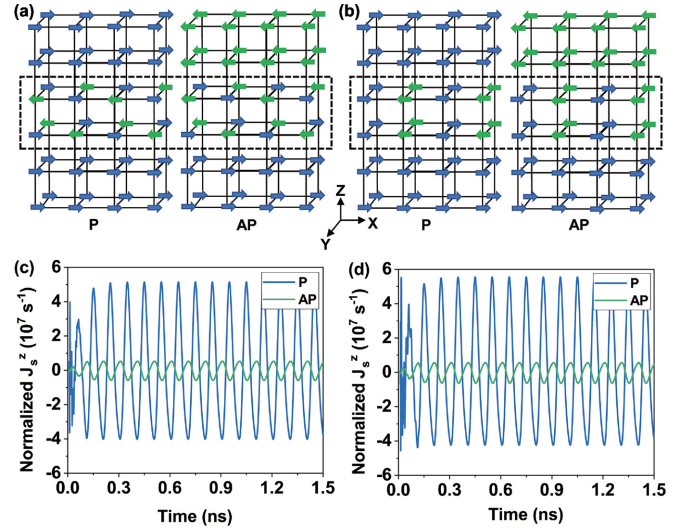


FIG. 2. (a) Structure of the magnon junction with the AFMI of (a) type A and (b) type C. (c) and (d) exhibit the z component of spin current density in a magnon junction for the parallel and antiparallel states with the AFMI spacers of type A and type C, respectively. Here, the spin current density was normalized by dividing the factor $\frac{\hbar}{4\pi} \text{Re}[g'_{\uparrow\downarrow}]$.

of magnetic moments along the [111] and [001] directions of NiO, respectively [34,43]. The magnetic structures of the magnetic junction composed by these two types of AFMI systems are presented in Figs. 2(a) and 2(b), including the parallel and antiparallel alignments of magnetic moments in the two FMI layers. (For simplicity, we only exhibited two magnetic-moment layers along the z -axis direction in each medium.) The bottom layer represents FMI1, with a fixed magnetic-moment orientation along the x -axis direction. The top two layers represent FMI2, and the magnetic moments in FMI2 can be parallel or antiparallel to that in FMI1.

Figures 2(c) and 2(d) depict the temporal spin current densities at the FMI2/Pt interface for parallel and antiparallel states with the two types of AFMI spacers. We observed a substantial reduction in the amplitude of the spin current density for the antiparallel state in both AFMI structures. Furthermore, a clear nonzero average spin current density was noticeable for the parallel state, whereas the antiparallel state displayed a negligible average net spin current density. Based on Eqs. (8)–(10), the U_{ISHE} at the parallel state for type A and C were 5.2 and 5.5 μV , respectively, while it is virtually 0 μV at the antiparallel state for both types. This corresponds to a 100% MBR, which signifies the effective regulation of magnon current transmission in the magnon junction by alternating the orientation of the magnetic moments in FMI2 layers.

The magnon junction effect was thought to be relevant to the chirality-relevant magnon scattering at the FMI/AFMI interface. This principle assumes two paths for the magnon propagation with opposite chiralities in the AFMI spacer, which appears to be inspired by the parallel circuit model for explaining the giant magnetoresistance (GMR) effect. When the magnetic moments in the two FMI layers are parallel, the magnon current transporting in one of the two paths conserves

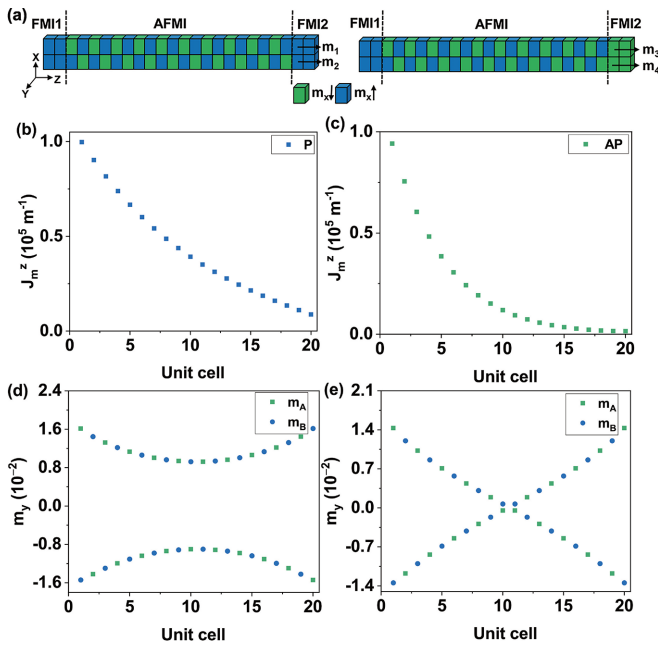


FIG. 3. (a) x component of AFMI magnetic moment in equilibrium for the parallel (left) and antiparallel (right) states. Normalized spin current density at different positions in the AFMI spacer for the (b) parallel and (c) antiparallel state. y -component magnetic moment at different positions in the AFMI spacer for the (d) parallel and (e) antiparallel states.

chirality and experiences weaker scattering. Nevertheless, when the magnetic moments in the two FMI layers are antiparallel, strong magnon scattering occurs in both paths due to the sharp variation for the chirality of magnetic oscillation at either the left or right FMI/AFMI interface [6]. This may be reasonable for the magnon junction effect in the magnon junction with a type-C AFMI structure, since the two paths for the magnon current with opposite chiralities are separated [see Fig. 1(d) in Ref. [6] and Fig. 4(a)]. However, this principle may not be quite easy to explain in the junction with type-A AFMI, as the magnetic oscillations with opposite chiralities are mixed in either path along the thickness direction of the AFMI spacer [see Fig. 2(g) in Ref. [6] and Fig. 3(a)]. To satisfy the transmission of magnon current along the path with a fixed chirality, one has to assume the reorientation for the flow of magnon current as indicated in Fig. 2(h) of Ref. [6]. However, this complicated magnon current flow within the AFMI spacer is challenging to verify in experiment.

In this paper, we proposed a different mechanism for explaining the magnon junction effect by taking into account different magnetic structures in the AFMI spacer between the parallel and antiparallel states. We first considered the magnon current transmission along the z -axis direction in the magnon junction with type-A AFMI. We noticed that when the magnon junction is in a parallel state, the spin current inside AFMI decays smoothly as compared to that in an antiparallel state [Figs. 3(b) and 3(c)]. In the antiparallel state, however, the spin current significantly decays in the left half of the AFMI layer [Fig. 3(c)].

We further examined the m_y in equilibrium within the AFMI medium at different positions from left to right (m_z

is not shown here since it does not contribute to J_s^z). In the parallel state, the variation of m_y in the AFMI spacer is limited in a small range without the variation of sign [Fig. 3(d)]. In contrast, in the antiparallel state, a domain-wall-like structure forms within the AFMI spacer, and the m_y diminishes as it approaches the center of the AFMI spacer [Fig. 3(e)]. This indicates that the magnetic moment in the middle of the AFMI spacer aligns strictly along the easy-axis direction (x direction). In general, a small initial deviation for the alignment of magnetic moments from the easy axis is necessary for triggering magnetic oscillation. Otherwise, the magnetic oscillation is inhibited by the strong anisotropy field. This deviation can be realized by applying an external magnetic field along the hard axis (the y and z axis) or by thermal fluctuation. In this work, under the hard-axis magnetic field, all the AFMI magnetic moments deviate from the easy axis for the parallel state, but the magnetic moment in the middle of the AFMI spacer is still along the easy axis for the antiparallel state. Therefore, the magnetic oscillation in the middle of the AFMI spacer is depressed for the antiparallel state. This blocks magnon current transmission.

Similar results were also observed in the magnon junction with a C-type AFMI spacer, as illustrated in Figs. 4(a)–4(e). Distinct from the alternative arrangement of positive and negative m_x in the A-type counterpart, in the C-type AFMI form, the positive and negative m_x comprise two separated paths for magnon transport with opposite chiralities. To reveal the contribution of magnon current with opposite chiralities to the magnon junction effect, we analyzed the oscillation of a pair of magnetic moments at the first unit cell in the AFMI at the parallel state [Figs. 4(f) and 4(g)]. Here, m_L and m_R indicate the magnetic precession with the left-handed modes (LHMs) and right-handed modes (RHMs). As observed in Fig. 4(g), the amplitude for the oscillation of m_R is a little larger than that of m_L in Fig. 4(f).

We also calculated the magnon spin current densities at the grid points $m_{1(L)}$, $m_{2(R)}$, $m_{3(L)}$, and $m_{4(R)}$ as designated in Figs. 4(h) and 4(i). In the parallel state, the average densities for the spin current in $m_{1(L)}$ and $m_{2(R)}$ are 0.239×10^4 and $0.245 \times 10^4 \text{ m}^{-1}$ (exchange spin current of FMI, normalized by A_{ex}), respectively. In the antiparallel state, the magnon currents transmitted to $m_{3(L)}$ is slightly weaker than that in $m_{4(R)}$ (5.7 m^{-1} for $m_{3(L)}$ and 5.8 m^{-1} for $m_{4(R)}$) (normalized by A_{ex}). Indeed, the spin current density for the magnon current with opposite chiralities is different. However, this difference is negligible as compared to that for the magnon current between the parallel and antiparallel states. This verifies that the chirality-relevant magnon scattering is not be the main reason for the magnon junction effect, and the blocking of the magnon spin current mainly happens in the middle of the AFMI spacer rather than at the FMI/AFMI interface.

Finally, to verify that the important role the AFMI magnetic structure plays in controlling the magnon current transmission is suitable for a general situation, we added the simulation under different boundary conditions (BCs) for the exchange coupling at the FM/AFM interface [Figs. 5(a) and 5(b)]. These BCs include the compensated BC and the uncompensated BCs for the FM and AFM exchange coupling at the AFMI/FMI interface [19,24,44–48]. We also considered the magnetic structure in the AFMI spacer and the z

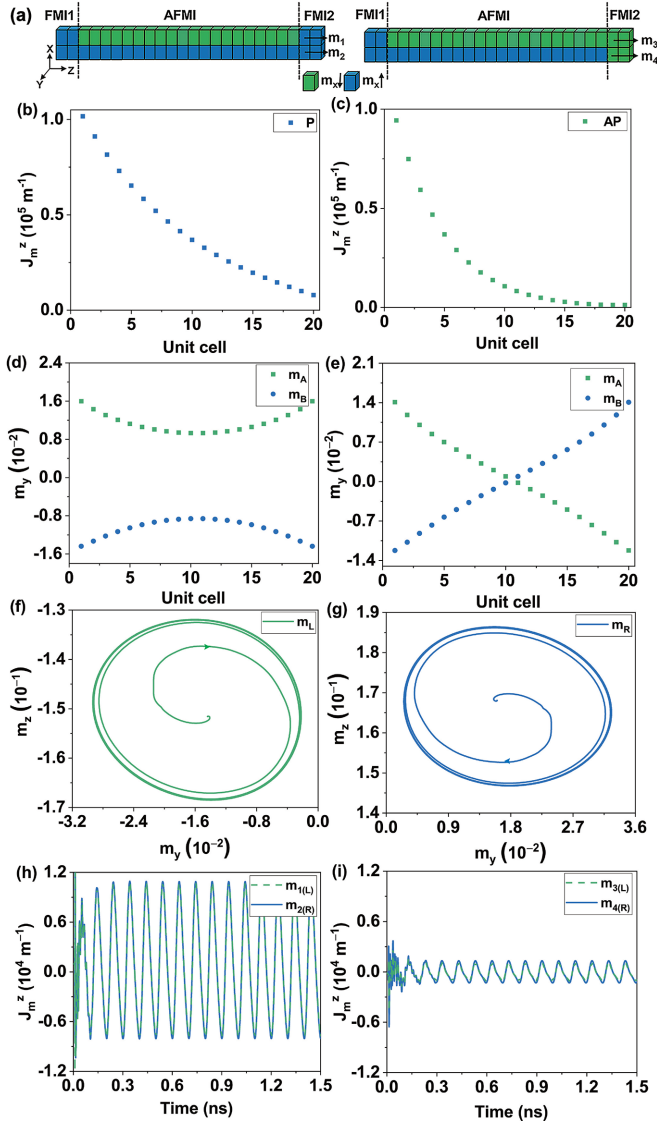


FIG. 4. (a) x component of an AFMI magnetic moment in parallel and antiparallel states. (b) and (c) Magnon spin current density in the AFMI layer at different positions for the parallel and antiparallel states, respectively. (d) and (e) y -component magnetic moment in the AFMI spacer at different positions for the parallel and antiparallel states, respectively. (f) and (g) Magnetic precession of the first unit cell from the left in AFMI in the parallel state. (h) and (i) z -component spin current density of the first unit cell from the left in FMI2 in the parallel and antiparallel states, respectively.

component of spin current density under different magnetic fields along the hard axis [Figs. 5(c) and 5(d)]. One can see a similar alignment of AFMI magnetic moments for the parallel and antiparallel states under all the BCs, and the magnon transmission is generally inhibited when there are AFMI magnetic moments aligning strictly along the easy axis. Therefore,

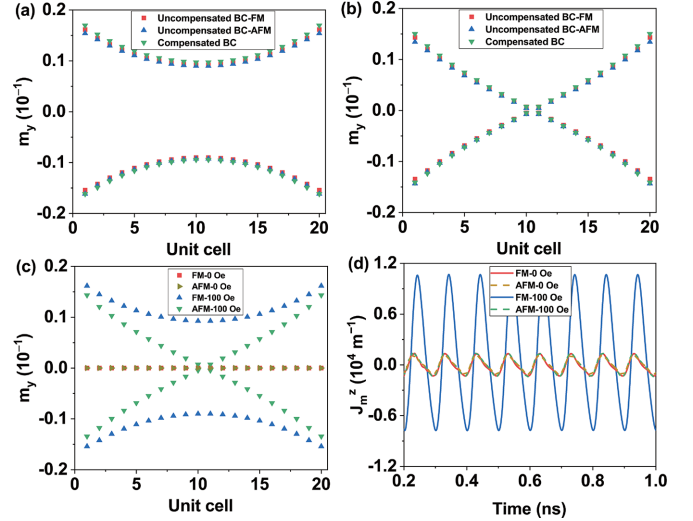


FIG. 5. (a) and (b) y component of the magnetic moments in the AFMI spacer under different AFMI/FMI boundary conditions for the parallel and antiparallel states, respectively. (c) and (d) y component of the magnetic moments in the AFMI spacer and z component of the spin current density at the first unit cell from the left in FMI2 under different magnetic fields for the FM and AFM coupling at the AFMI/FMI interface, respectively.

we can safely conclude that the magnetic structure of the AFMI spacer indeed makes a generally significant impact on the magnon transmission.

IV. CONCLUSIONS

We have studied the magnon junction effect induced by a bulk acoustic wave. Our numerical results reveal significant control over the magnon current density in a magnon junction triggered by a bulk acoustic wave. The manipulation of the magnetic moments within ferromagnetic insulator layers allows us to completely block transmission in antiparallel alignments. The critical mechanism for the blocking effect lies in the strict alignment of magnetic moments along the easy axis in the midsection of the antiferromagnetic spacer. Our study provides insights into the magnon junction effect and advances the development of on-chip magnonics devices.

ACKNOWLEDGMENTS

Q.F. and Y.Z. acknowledge the financial support from the National Natural Science Foundation of China (Grants No. 61971459 and No. 51971098) and Shenzhen Technology Plan (JCYJ20190809095009521).

There are no conflicts to declare.

- [1] M. N. Baibich, J. M. Broto, A. Fert, F. Nguyen Van Dau, F. Petroff, P. Etienne, G. Creuzet, A. Friederich, and J. Chazelas, *Phys. Rev. Lett.* **61**, 2472 (1988).
- [2] G. Binasch, P. Grunberg, F. Saurenbach, and W. Zinn, *Phys. Rev. B* **39**, 4828 (1989).
- [3] J. S. Moodera, L. R. Kinder, T. M. Wong, and R. Meservey, *Phys. Rev. Lett.* **74**, 3273 (1995).
- [4] H. Wu, L. Huang, C. Fang, B. S. Yang, C. H. Wan, G. Q. Yu, J. F. Feng, H. X. Wei, and X. F. Han, *Phys. Rev. Lett.* **120**, 097205 (2018).
- [5] C. Y. Guo, C. H. Wan, X. Wang, C. Fang, P. Tang, W. J. Kong, M. K. Zhao, L. N. Jiang, B. S. Tao, G. Q. Yu, and X. F. Han, *Phys. Rev. B* **98**, 134426 (2018).
- [6] Z. R. Yan, C. H. Wan, and X. F. Han, *Phys. Rev. Appl.* **14**, 044053 (2020).
- [7] A. V. Azovtsev and N. A. Pertsev, *Phys. Rev. B* **94**, 184401 (2016).
- [8] A. V. Azovtsev and N. A. Pertsev, *Appl. Phys. Lett.* **111**, 222403 (2017).
- [9] A. V. Azovtsev and N. A. Pertsev, *Phys. Rev. B* **100**, 224405 (2019).
- [10] W. Al Misba, M. M. Rajib, D. Bhattacharya, and J. Atulasimha, *Phys. Rev. Appl.* **14**, 014088 (2020).
- [11] B. Casals, N. Statuto, M. Foerster, A. Hernandez-Minguez, R. Cicheler, P. Manshausen, A. Mandziak, L. Aballe, J. M. Hernandez, and F. Macia, *Phys. Rev. Lett.* **124**, 137202 (2020).
- [12] D. Kobayashi, T. Yoshikawa, M. Matsuo, R. Iguchi, S. Maekawa, E. Saitoh, and Y. Nozaki, *Phys. Rev. Lett.* **119**, 077202 (2017).
- [13] K. Uchida, H. Adachi, T. An, T. Ota, M. Toda, B. Hillebrands, S. Maekawa, and E. Saitoh, *Nat. Mater.* **10**, 737 (2011).
- [14] M. Weiler, H. Huebl, F. S. Goerg, F. D. Czeschka, R. Gross, and S. T. B. Goennenwein, *Phys. Rev. Lett.* **108**, 176601 (2012).
- [15] J. Cramer, F. Fuhrmann, U. Ritzmann, V. Gall, T. Niizeki, R. Ramos, Z. Qiu, D. Hou, T. Kikkawa, J. Sinova, U. Nowak, E. Saitoh, and M. Klau, *Nat. Commun.* **9**, 1089 (2018).
- [16] W. He, H. Wu, C. Guo, C. Wan, M. Zhao, Y. Xing, P. Tang, Z. Yan, J. Xia, T. Yu, and X. Han, *Appl. Phys. Lett.* **119**, 212410 (2021).
- [17] Z. Li, X. Zhang, D. Zhang, B. Liu, H. Meng, J. Xu, Z. Zhong, X. Tang, H. Zhang, and L. Jin, *APL Mater.* **10**, 021101 (2022).
- [18] G. Vilela, H. Chi, G. Stephen, C. Settens, P. Zhou, Y. Ou, D. Suri, D. Heiman, and J. S. Moodera, *J. Appl. Phys.* **127**, 115302 (2020).
- [19] V. Brehm, M. Evers, U. Ritzmann, and U. Nowak, *Phys. Rev. B* **105**, 104408 (2022).
- [20] R. F. Evans, W. J. Fan, P. Chureemart, T. A. Ostler, M. O. Ellis, and R. W. Chantrell, *J. Phys.: Condens. Matter* **26**, 103202 (2014).
- [21] F. Chen, X. Ge, W. Luo, R. Xing, S. Liang, X. Yang, L. You, R. Xiong, Y. Otani, and Y. Zhang, *Phys. Rev. Appl.* **15**, 014030 (2021).
- [22] K. Lee, D. K. Lee, D. Yang, R. Mishra, D. J. Kim, S. Liu, Q. Xiong, S. K. Kim, K. J. Lee, and H. Yang, *Nat. Nanotechnol.* **16**, 1337 (2021).
- [23] A. Vansteenkiste, J. Leliaert, M. Dvornik, M. Helsen, F. Garcia-Sanchez, and B. Van Waeyenberge, *AIP Adv.* **4**, 107133 (2014).
- [24] M. Finazzi, *Phys. Rev. B* **69**, 064405 (2004).
- [25] H. J. Koo, H. Xiang, C. Lee, and M. H. Whangbo, *Inorg. Chem.* **48**, 9051 (2009).
- [26] F. Wu, E. Kan, C. Tian, and M. H. Whangbo, *Inorg. Chem.* **49**, 7545 (2010).
- [27] G. Consolo, G. Valenti, A. R. Safin, S. A. Nikitov, V. Tyberkevich, and A. Slavin, *Phys. Rev. B* **103**, 134431 (2021).
- [28] P. Yan, X. S. Wang, and X. R. Wang, *Phys. Rev. Lett.* **107**, 177207 (2011).
- [29] V. Baltz, A. Manchon, M. Tsoi, T. Moriyama, T. Ono, and Y. Tserkovnyak, *Rev. Mod. Phys.* **90**, 015005 (2018).
- [30] R. Cheng, D. Xiao, and A. Brataas, *Phys. Rev. Lett.* **116**, 207603 (2016).
- [31] R. Cheng, J. Xiao, Q. Niu, and A. Brataas, *Phys. Rev. Lett.* **113**, 057601 (2014).
- [32] J. Han, R. Cheng, L. Liu, H. Ohno, and S. Fukami, *Nat. Mater.* **22**, 684 (2023).
- [33] J. Han, P. Zhang, Z. Bi, Y. Fan, T. S. Safi, J. Xiang, J. Finley, L. Fu, R. Cheng, and L. Liu, *Nat. Nanotechnol.* **15**, 563 (2020).
- [34] E. G. Tveten, A. Qaiumzadeh, and A. Brataas, *Phys. Rev. Lett.* **112**, 147204 (2014).
- [35] L. Jin, K. Jia, D. Zhang, B. Liu, H. Meng, X. Tang, Z. Zhong, and H. Zhang, *ACS Appl. Mater. Interfaces* **11**, 35458 (2019).
- [36] E. Lesne, Y. Fu, S. Oyarzun, J. C. Rojas-Sanchez, D. C. Vaz, H. Naganuma, G. Sicoli, J. P. Attane, M. Jamet, E. Jacquet, J. M. George, A. Barthelemy, H. Jaffres, A. Fert, M. Bibes, and L. Vila, *Nat. Mater.* **15**, 1261 (2016).
- [37] H. J. Jiao and G. E. W. Bauer, *Phys. Rev. Lett.* **110**, 217602 (2013).
- [38] E. Shikoh, K. Ando, K. Kubo, E. Saitoh, T. Shinjo, and M. Shiraishi, *Phys. Rev. Lett.* **110**, 127201 (2013).
- [39] T. Kimura, Y. Otani, T. Sato, S. Takahashi, and S. Maekawa, *Phys. Rev. Lett.* **98**, 156601 (2007).
- [40] J. C. Rojas-Sanchez, N. Reyren, P. Laczkowski, W. Savero, J. P. Attane, C. Deranlot, M. Jamet, J. M. George, L. Vila, and H. Jaffres, *Phys. Rev. Lett.* **112**, 106602 (2014).
- [41] J. Walowski and M. Münzenberg, *J. Appl. Phys.* **120**, 140901 (2016).
- [42] A. Mekonnen, M. Cormier, A. V. Kimel, A. Kirilyuk, A. Hrabec, L. Ranno, and T. Rasing, *Phys. Rev. Lett.* **107**, 117202 (2011).
- [43] W. L. Roth, *J. Appl. Phys.* **31**, 2000 (1960).
- [44] J. De Clercq, J. Leliaert, and B. Van Waeyenberge, *J. Phys. D* **50**, 425002 (2017).
- [45] A. G. Grechnev and A. S. Kovalev, *Low Temp. Phys.* **24**, 629 (1998).
- [46] Y. Li, T. X. Wang, H. Y. Liu, X. W. Xu, Z. M. Lu, and Y. X. Li, *Eur. Phys. J. B* **66**, 369 (2008).
- [47] T. C. Schulthess and W. H. Butler, *J. Appl. Phys.* **85**, 5510 (1999).
- [48] S.-H. Tsai, D. P. Landau, and T. C. Schulthess, *J. Appl. Phys.* **93**, 8612 (2003).